Measurement Science and Technology

100 year anniversary
Measurement Science and Technology

PAPER

Investigation of textured sensing skin for monitoring fatigue cracks on fillet welds

To cite this article: Han Liu *et al* 2022 *Meas. Sci. Technol.* **33** 084001

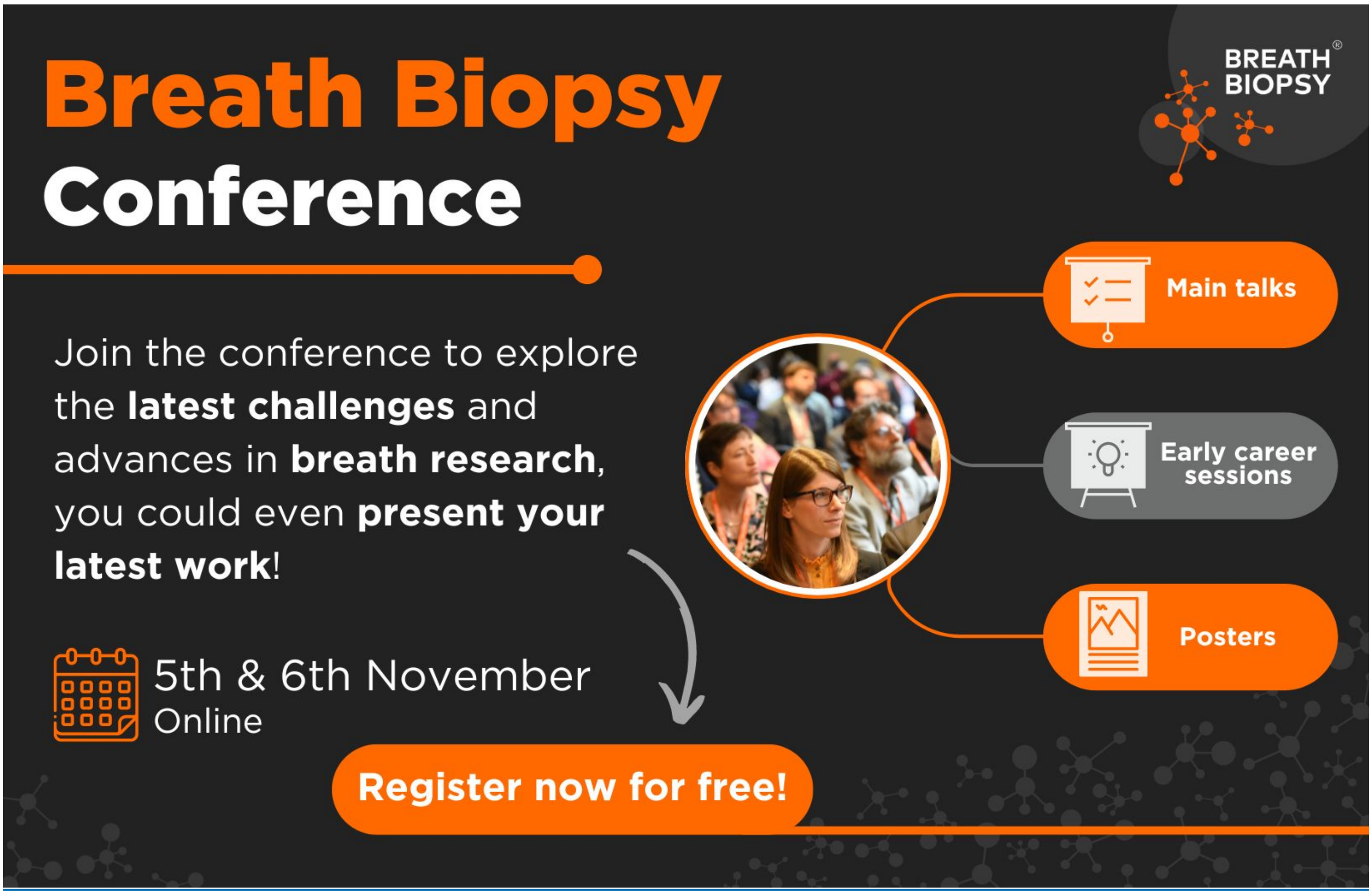

Meas. Sci. Technol. 33 (2022) 084001 (17pp) https://doi.org/10.1088/1361-6501/ac6935

Investigation of textured sensing skin for monitoring fatigue cracks on fillet welds

Han Liu[1,*], Simon Laflamme[1,2], Jian Li[3], Caroline Bennett[3], William N Collins[3], David J Eisenmann[4], Austin R J Downey[5,6], Paul Ziehl[5,6] and Hongki Jo[7]

[1] Department of Civil, Construction and Environmental Engineering, Iowa State University, Ames, IA, United States of America
[2] Department of Electrical and Computer Engineering, Iowa State University, Ames, IA, United States of America
[3] Department of Civil, Environmental and Architectural Engineering, The University of Kansas Lawrence, KS, United States of America
[4] Department of Agricultural and Biosystems Engineering, Iowa State University, Ames, IA, United States of America
[5] Department of Mechanical Engineering, University of South Carolina, Columbia, SC, United States of America
[6] Department of Civil and Environmental Engineering, University of South Carolina, Columbia, SC, United States of America
[7] Department of Civil, Architectural Engineering and Mechanics, The University of Arizona, Tucson, AZ, United States of America

E-mail: liuhan@iastate.edu

Received 20 December 2021, revised 8 April 2022
Accepted for publication 21 April 2022
Published 5 May 2022

Abstract

Load-induced fatigue cracking in welds is a critical safety concern for steel transportation infrastructure, and the automation of their detection using commercial sensing technologies remains challenging due to the randomness in crack initiation and propagation. The authors have previously proposed a corrugated soft elastomeric capacitor (cSEC), which is a flexible and ultra-compliant thin-film strain gauge that transduces strain into a measurable change in capacitance. The cSEC technology has been successfully demonstrated for measuring bending strain as well as angular rotation in a folded configuration. This study builds on prior discoveries to characterize the sensor's capability at monitoring fatigue cracks in corner welds, for which the sensor needs to be installed in a folded configuration. A crack monitoring algorithm is developed to fuse the cSEC data into actionable information. Experimental work is conducted on an orthogonal welded connection, mimicking a plate-to-web joint in steel bridges, with cSECs folded over the fillet welds. The sensor's electromechanical behavior is characterized, and results confirm that the cSEC is capable of fatigue crack detection and quantification. In particular, results show that the cSEC can detect a minimum crack length of 0.48 mm and that its overall sensing performance, including signal linearity, resolution, and accuracy, is adequate under no damage, yet decreases with increasing crack size, likely attributable to the simplification of the electromechanical model and higher noise produced by the loading equipment under smaller applied displacement.

* Author to whom any correspondence should be addressed.

Keywords: fatigue crack, flexible strain gauge, structural health monitoring, sensing skin, fillet weld, joint connection, complex geometry

(Some figures may appear in colour only in the online journal)

1. Introduction

Fatigue-induced cracks forming on steel components is one of the primary safety concerns associated with deterioration of transportation infrastructure [1]. These cracks, if not detected and addressed in a timely manner, can have grave consequences, including brittle structural failures [2, 3]. It is estimated that close to half of the nation's bridges have at least one load-induced fatigue crack reported on welds, gusset plates, riveted built-up members, or girders [4]. Of interest to this paper are cracks forming at welded connections. Welding is a practical joining method widely employed in the fabrication of steel bridge components (e.g. assemble beams, channels, angles, plates, and other metal components) due to its low cost and reliability. However, the effect of service loads combined with residual stresses generated from the fast heating and cooling cycles during the welding process can significantly accelerate the formation of fatigue cracks [5].

Despite the fact that the importance of fatigue weldment cracking has been recognized and that numerous relevant research investigations have been conducted and reported since the 1920s [6], the detection of fatigue cracking in welds still mainly relies on visual inspections [7–9] and nondestructive evaluation (NDE) techniques (e.g. thermography [10], ultrasonic testing [11], x-ray imaging [12, 13], magnetic particle testing [14], eddy-current testing [15], acoustic emission monitoring [16–18]). However, both approaches usually require a trained practitioner, and timely detection is limited by the inspection schedule and quality of the inspection and/or NDE process.

Structural health monitoring (SHM) can be used to automate the task of fatigue crack discovery by strategically designing and deploying dedicated sensor networks. Large-area electronics (LAE) [19, 20] is a particularly promising technology by enabling sensing skin-type applications through the deployment of dense sensor networks covering large surfaces and capable of local measurements, thus facilitating fatigue crack detection over full-scale components [21, 22]. Specific examples of dense sensor networks include an eddy current sensor array fabricated by integrating an actuating coil and a sensing coil into a flexible printed circuit board [23] applied to welds, ultrasonic guided wave-based piezoelectric lead zirconate titanate disks supported by a thin flexible dielectric film used for diagnosis and assessment of fatigue cracks in the weld of a T-shape bogie frame [24], a mechanoluminescent sensor fabricated by coating $SrAl_2O_4$:Eu ceramic powder on an aluminum foil through screen-printing to detect cracks on welding points located on the outside surface of a pressurized pipe [25], fiber Bragg grating sensors used for discovering and localizing cold cracks in welded areas of steel plates [26], and commercial piezoelectric sensor networks applied to monitor weld cracks on T-type joints in steel offshore oil and gas jacket platforms [27] and metro train bogie frames [28].

The authors have recently proposed a corrugated soft elastomeric capacitor (cSEC) that is a thin-film flexible sensor of high compliance and scalability. The cSEC is a parallel plate capacitor that transduces strain into a measurable change in capacitance with a reported resolution of 25 $\mu\varepsilon$ [29]. It is fabricated by infilling titania (TiO_2) and carbon black (CB) particles into a styrene-ethylene-butylene-styrene (SEBS) block copolymer matrix to form the dielectric layer and conductive plates, respectively, and layering them into a sandwiched structure. Notably, the cSEC technology has been characterized and demonstrated for in-plane fatigue crack monitoring and out-of-plane angular motion sensing [30, 31]. Compared to conventional strain sensors such as foil gauges, the cSEC covers and senses over large areas and can thus be used to discover new cracks instead of being exclusively used to monitor existing damage.

Unlike the case of uniform in-plane strain that can be verified experimentally, non-uniform strain occurring on welded structural components under distortion is difficult to quantify. In this paper, we investigate the utilization of the cSEC to detect and monitor fatigue cracks in welded corners subjected to angular rotation, in particular for the sensor installed in a folded configuration for strain-based measurements (see figure 6(c)). The test is performed on a steel specimen assembled using a three-pass horizontal fillet weld applied manually along the edges of two steel angles to create welded corners and form a square box. The load-induced shear force and angular rotation-induced bending strain drives the initiation and extension of fatigue cracks at the welds. A high-cycle fatigue load regime is used to accelerate damage initiation and extend damage sizes. The objective is to characterize the cSEC signal when performing such a task, anticipating that discoveries will be useful to applications in the field and over complex geometries. A revised electromechanical model is developed based on a bending model and validated by comparing it against numerical and experimental results. The sensing performances are characterized and quantified for high-cycle fatigue cracks, and a crack monitoring algorithm integrating angular rotation index (ARI) and crack growth index (CGI) is proposed to fuse measurements into a scalar associated with crack size.

The rest of this paper is organized as follows. Section 2 provides the background which includes bending deformation and fatigue cracks at fillet welds, cSEC technology, the derivation of the electromechanical model suitable for bending deformation. The algorithm used for finite element (FE) analysis and the proposed intelligent crack monitoring algorithm are also demonstrated in this section. Section 3 presents the methodology used in this study, including a description of the damage law, numerical model, fatigue load protocols, and the experimental procedure. Section 4 presents and discusses results of the Paris' coefficients, numerical model validation, signal study, crack monitoring, and sensing performance evaluation. Section 5 concludes the paper by summarizing key findings and discussing future work.

2. Background

This section provides the necessary background on the cSEC technology, the associated electromechanical model, the finite element model (FEM) used for simulating capacitance variations, and the algorithm used in discovering and quantifying fatigue crack in corner welds.

2.1. cSEC technology

Figure 1(a) presents a square cSEC with a reinforced diagrid pattern. A cSEC is a robust LAE that is inexpensive and easy to fabricate. Its design, fabrication process, and electromechanical model for in-plane strain monitoring are described in detail in [29] and briefly reviewed here for completeness. Its sensing principle is based on a change in the monitored area causing geometric deformation of the sensor that provokes a measurable change in its capacitance. The cSEC takes the form of a parallel plate capacitor constituted by a dielectric layer with conductive plates, as shown in figure 1(b). The dielectric is composed of a SEBS block co-polymer matrix filled with PDMS-coated titania (TiO_2) for enhancing its durability and permittivity. The conductive plates are fabricated by using the same SEBS but filled with CB particles to provide conductivity, painted onto each side of the dielectric. Two self-adhesive copper tabs are added to the conductors on both the top and bottom plates to create electrical connections that are used to connect to the data acquisition system (DAQ) through soldering. Lastly, a thin layer of PELCO conductive glue is applied over the copper tabs to ensure a good connection between the copper contacts and the conductors.

2.2. Electromechanical model

The cSEC can be modeled as a non-lossy parallel plate capacitor under low-frequency measurement (<1 kHz) with the initial capacitance C_0 written as:

$$C_0 = e_0 e_r \frac{A}{h} \tag{1}$$

where $e_0 = 8.854\ \mathrm{pF\,m^{-1}}$ is the vacuum permittivity of the sensor, e_r its relative permittivity, h the thickness of the dielectric, and $A = l \cdot d$ the electrode area of length l and width d, as denoted in figure 1(b).

For plate-to-web welded connections such as those at a cross-frame or diaphragm connection plate (e.g. T-joints and cross-joints) angular rotation induced bending deformation is typically generated around the welding zone, particularly where out-of-plane loads are not applied perfectly orthogonally with respect to the web. Therefore, higher-order strain terms $\varepsilon_x \times \varepsilon_y$ and out-of-plane strain ε_z need to be considered to characterize the capacitance response and establish the relationship between $\Delta C/C_0$ and bending strain.

Strain can be considered as uniformly distributed over a small unit volume of an cSEC of initial length l, width w, and thickness h, as shown in figure 2(a). The unit volume will deformed to length l', width w', and thickness h', with the relative change in capacitance $\Delta C/C_0$ expressed as:

$$\frac{\Delta C}{C_0} = \frac{C_1 - C_0}{C_0} = \frac{e_0 e_r \left(\frac{A'}{h'} - \frac{A}{h}\right)}{e_0 e_r \frac{A}{h}} = \frac{A'h - Ah'}{Ah'} \tag{2}$$

where C_1 is the final capacitance value of the cuboid unit and A' is the sensing area of the unit after deformation. Substituting $A = lw$ and $A' = l'w'$ into equation (2) gives

$$\frac{\Delta C}{C_0} = \frac{l'w'h - lwh'}{lwh'}. \tag{3}$$

Differentiating equation (3) with respect to length l and width w, the capacitance response $\Delta C/C_0$ of the sensor becomes:

$$\frac{\Delta C}{C_0} = \left(\frac{l'-l}{l} + \frac{w-w'}{w} - \frac{h-h'}{h}\right) = \varepsilon_x + \varepsilon_y - \varepsilon_z \tag{4}$$

where ε_x and ε_y are the in-plane strains and ε_z is the out-of-plane strain, as shown in figure 1(b). Substituting $l' = (1+\varepsilon_x)l$, $w' = (1+\varepsilon_y)w$, and $h' = (1+\varepsilon_z)h$ into equation (4), one obtains

$$\frac{\Delta C}{C_0} = \frac{(1+\varepsilon_x)(1+\varepsilon_y)}{1+\varepsilon_z} - 1. \tag{5}$$

Using Hooke's Law under plane stress assumption, for a plain (isotropic) SEC with Poisson's ratio ν, the strain along the z-axis can be written as

$$\begin{aligned} \varepsilon_z &= -\frac{\nu}{E}(\sigma_x + \sigma_y) = -\frac{\nu}{1-\nu}(\varepsilon_x + \varepsilon_y) \\ &= \frac{1}{(1+\varepsilon_x)(1+\varepsilon_y)} - 1. \end{aligned} \tag{6}$$

Substituting equation (6) into equation (5) yields

$$\frac{\Delta C}{C_0} = (1+\varepsilon_x)^2(1+\varepsilon_y)^2 - 1. \tag{7}$$

The corrugated surface alters the stiffness of the dielectric layer in the $x-y$ plane and yields with a transverse Poisson's ratio ν_{xy} expressed, in a free-standing configuration, as

$$\nu_{xy} = -\frac{\varepsilon_y}{\varepsilon_x}. \tag{8}$$

When the sensor is fully adhered onto the monitored material, the composite effect on ν_{xy} needs to be considered (e.g. stiffness of the monitored material and level of adhesion).

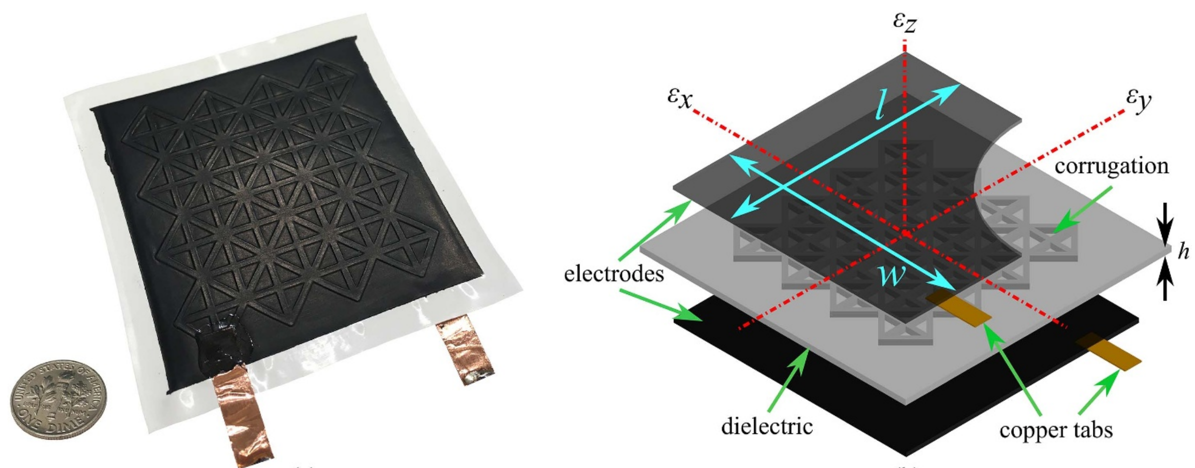

Figure 1. (a) Picture of a 76 mm × 76 mm cSEC with a reinforced diagrid pattern; and (b) schematic showing the architecture of a cSEC of thickness h and a section of the electrode layer with electrode area $l \times w$ (black layer).

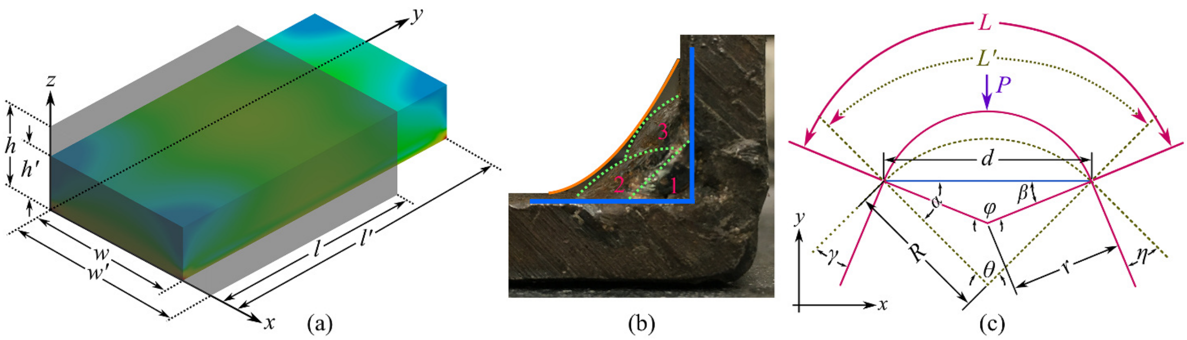

Figure 2. Schematic drawings showing: (a) small cuboid unit of a cSEC with an initial length of l, width of w, and thickness of h; (b) section view of the corner welded using a three-pass fillet weld showing three segments; and (c) comparison of the arc's deformation with and without an applied compressive load.

Here, the transverse Poisson's ratio under composite action $\nu_{xy,c}$ can be taken as

$$\nu_{xy,c} = -\frac{a\nu_{xy} + b\nu_m}{a+b} = -\frac{\varepsilon_{y,c}}{\varepsilon_{x,c}} \tag{9}$$

where ν_m is the Poisson's ratio of monitored material, $0 \leqslant a \leqslant 1$ and $0 \leqslant b \leqslant 1$ are weights such that $a + b = 1$, and $\varepsilon_{x,c}$ and $\varepsilon_{y,c}$ are the in-plane strains in x and y directions under composite action. When applied to steel, as it is the case in this study, $a \approx 0$ and $b \approx 1$. Substituting equation (9) into equation (7) yields

$$\frac{\Delta C}{C_0} = (1+\varepsilon_{x,c})^2(1-\nu_{xy,c}\cdot\varepsilon_{x,c})^2 - 1. \tag{10}$$

Numerical simulations conducted in a prior study [31] verified that up to 93.6% of the total elastic strain deformation ($\varepsilon_{x,c}$) in the sensor is distributed around the sensing area that is in contact with the curved corner under angular rotation-induced bending deformation. The electromechanical model of the cSEC under angular rotation deformation can be derived from the strain occurring along the arc length of the corner.

A three-pass horizontal fillet weld (also known as triple-pass horizontal fillet weld) was selected and used to assemble two L-shape channels along their edges to mimic a plate-to-web weld connection, producing a curved-like surface over the welded corners as shown in figure 1(b). Thus, in the model, the welded corners are simplified as curved arcs.

Figure 2(c) diagrams an arc of a initial arc angle φ, chord length d, arc radius r, and arc length L. The initial arc length L can be expressed as a function of the radius of curvature r and the intersection angle $\beta = (180° - \varphi)/2$

$$L = \varphi\cdot r = \varphi\cdot\frac{d\cdot\sin(\beta)}{\sin(\varphi)} = \eta\cdot\frac{d\cdot\sqrt{\frac{1-\cos(180°-\varphi)}{2}}}{\sin(\varphi)}. \tag{11}$$

Consider a concentrated load P acting at the vertex of the arc that results in angular rotations γ and η on the left-hand and right-hand sides, defined as the angles of rotation (also known as angle of inclination and angle of slope) between the x and y axes and the tangent at the tip of the deflected arcs in the x and y directions, respectively (presented in figure 2(c)). The initial central angle φ and radius r of the arc deform to θ and R under compression with the deformed arc angle θ written as a function of the angular rotations γ and η

$$\theta = \varphi - \gamma - \eta \tag{12}$$

with the deformed arc length L' written as

$$L' = \theta \cdot R = (\eta - \gamma - \eta) \cdot \frac{d \cdot \sin(\alpha)}{\sin(\theta)} = (\varphi - \gamma - \eta) \cdot \frac{d \cdot \sqrt{\frac{1-\cos(180^\circ - \varphi + \gamma + \eta)}{2}}}{\sin(\varphi - \gamma - \eta)} \tag{13}$$

and with

$$\alpha = \frac{180 - \theta}{2} = \frac{180^\circ - \varphi + \gamma + \eta}{2}. \tag{14}$$

The electromechanical model can be further refined by taking $\varepsilon_{x,c}$ in equation (10) as the bending strain ε_x written as a function of L and L' derived in equations (11) and (13):

$$\varepsilon_{x,c} = \varepsilon_x = \frac{\Delta L}{L} = \frac{L - L'}{L} = \frac{\left(\varphi \cdot \frac{d \cdot \sqrt{\frac{1-\cos(180^\circ - \varphi)}{2}}}{\sin(\varphi)} - (\varphi - \gamma - \eta) \cdot \frac{d \cdot \sqrt{\frac{1-\cos(180^\circ - \varphi + \gamma + \eta)}{2}}}{\sin(\varphi - \gamma - \eta)}\right)}{(\varphi - \gamma - \eta) \cdot \frac{d \cdot \sqrt{\frac{1-\cos(180^\circ - \varphi + \gamma + \eta)}{2}}}{\sin(\varphi - \gamma - \eta)}}. \tag{15}$$

2.3. Synthetic measurements

Equation (2) indicates that a change in the sensing area of the sensor will provoke a measurable change in its capacitance. Based on this sensing principle, the capacitance response of the sensor can be simulated by analyzing the deformation of the sensor through FEM simulations. To do so, the sensor is meshed through the tetrahedrons method (figure 5(a)) resulting in a total of P irregular mesh elements with each element partitioned into Q cuboids. The cuboids are considered small enough such that its strain is uniformly distributed. The capacitance response $\Delta C/C_0$ of a given cuboid (figure 2(a)) is derived as:

$$\frac{\Delta C^{p,q}}{C_0^{p,q}} = \left(1 + \varepsilon_{x,c}^{p,q}\right)^2 \left(1 - \nu_{xy,c}^{p,q} \cdot \varepsilon_{x,c}^{p,q}\right)^2 - 1 = \frac{A^{p,q}}{A_0^{p,q}} \tag{16}$$

where superscript p,q indicates quantities of the qth cuboid of the pth mesh element, and $A^{p,q}$ and $A_0^{p,q}$ are the deformed and initial area of the qth cuboid on the pth mesh element. The relative change in capacitance $\Delta C/C_0$ that arises in the entire meshed region can be computed by taking the summation of the capacitance response of every cuboid $\Delta C^{p,q}$:

$$\frac{\Delta C}{C_0} = \frac{1}{p \cdot q} \sum_{p=1}^{P} \sum_{q=1}^{Q} \frac{\Delta A^{p,q}}{A_0^{p,q}} = \frac{1}{p \cdot q} \sum_{p=1}^{P} \sum_{q=1}^{Q} \frac{\Delta C^{p,q}}{C_0^{p,q}}. \tag{17}$$

Figure 4(e) presents the normal elastic strain distribution on the sensor, which is numerically obtained from the FEM under compression and over a 0 mm crack ('no crack'). Applying equation (16) shows that up to 88.6% of the total elastic strain under the angular rotation is distributed around the sensing area in contact with the welded corner. This verifies prior assumption that the fillet welds can be treated as a curved surface in this study and that the electromechanical model of the cSEC under angular rotation occurred over corner welds can be derived only considering strain distributing along the arc length of the corner as derived in equations (11) and (15).

2.4. Crack monitoring algorithm

A real-time fatigue crack monitoring algorithm, diagrammed in figure 3, was developed to produce actionable data from measurements. A challenge in the algorithm is to decouple strain produced by angular rotation and that produced by a crack. First, the capacitance C measurement of the cSEC and load input F measured indirectly by other sensors (e.g. bending strain on a girder produced by a moving car) are initially collected, with the capacitance filtered using a low-pass filter to reduce high-frequency noise and eliminate capacitance drift that is caused by environmental factors (i.e. temperature and humidity) and intrinsic electrical behavior associated with many sensors fabricated from hyperelastic materials [32, 33]. The power spectral density (PSD) amplitudes of the cSEC ($\mathrm{PSD}_i^{\mathrm{m}}$) and load input sensor ($\mathrm{PSD}_i^{\mathrm{F}}$) are extracted and merged into an index termed ARI using [31]:

$$ARI_i = \frac{\mathrm{PSD}_i^{\mathrm{m}}}{\sqrt{\mathrm{PSD}_i^{\mathrm{F}}}}. \tag{18}$$

The ARI is a metric quantifying the level of angular rotation and relates linearly to the rotated angular degree with an accuracy of $\pm 0.416^\circ$. The rotated angular degree (θ_i) is mapped from the ARI and converted to bending strain (ε_B) using equation (15). Based on work in [31], there exists a linear relationship between the maximum amplitude of the PSD of the angular rotation ($\mathrm{PSD}_i^{\mathrm{r}}$) and ε_i, which allows the computation of $\mathrm{PSD}_i^{\mathrm{r}}$ directly from the bending strain ε_B. After, the PSD amplitude of the crack-induced signal (PSD_i^{c}) can be computed by subtracting ($\mathrm{PSD}_i^{\mathrm{r}}$) from the measured PSD amplitudes ($\mathrm{PSD}_i^{\mathrm{m}}$). Another metric, termed CGI_i^{c}), is written as equation $\frac{\sqrt{\mathrm{PSD}_i^{\mathrm{c}}}}{\sqrt{\mathrm{PSD}_i^{\mathrm{F}}}}$ [34]. Both ARI and CGI are metrics obtained by normalizing the numerators through taking the ratio to the square root of the peak force $\sqrt{\mathrm{PSD}_i^{\mathrm{F}}}$ to make their input-independent and represent the level of the peak-to-peak (P2P) capacitance amplitudes under a unit excitation load. However, the key difference is that the normalized numerators fuse

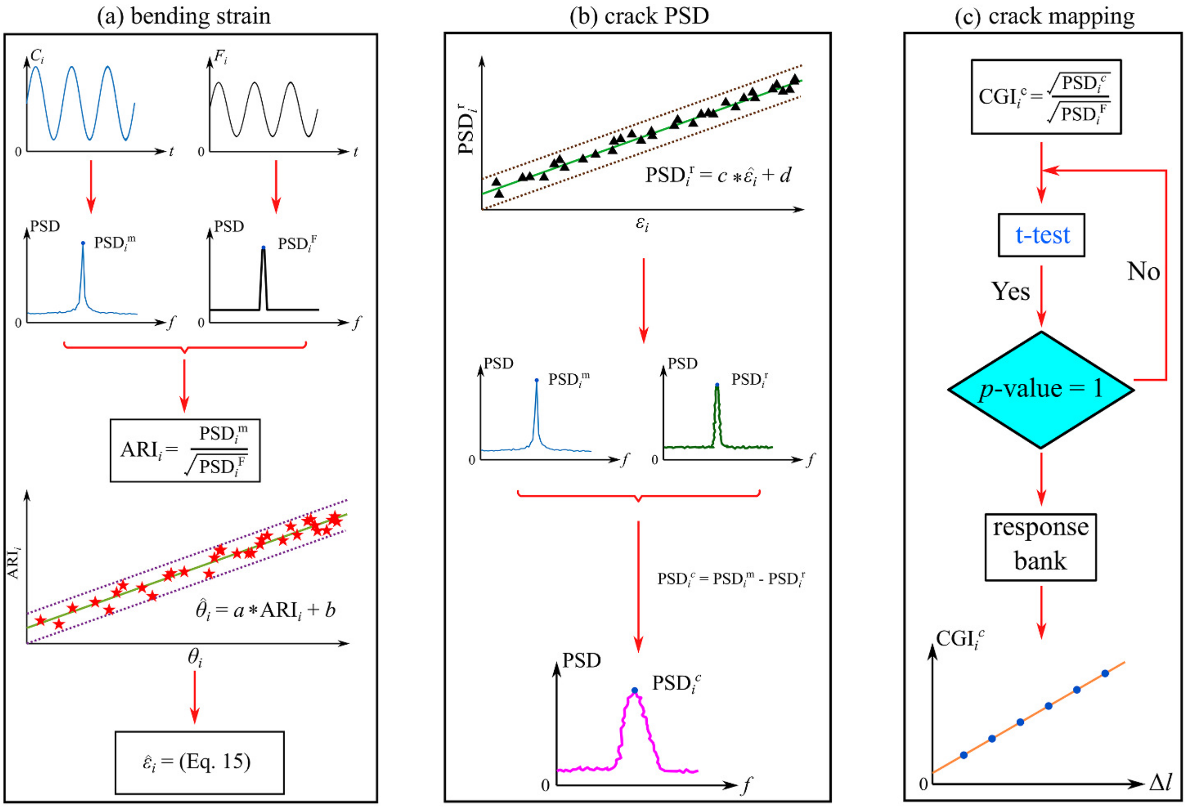

Figure 3. Schematic of the crack motoring algorithm framework.

different features, in which PSD_i^r and PSD_i^c are independently correlated with the level of the angular rotation and crack length at the *i*th measurement. A fatigue crack discovery can be determined by conducting a continuous paired t-test on CGI_i^c. The t-test would reject the null hypothesis and indicate a crack is discovered when the *p*-values are stabilized with a value of 1. Finally, the CGI_i^c data could be useful in SHM applications to directly quantify cracks and estimate crack growth rate by evaluating its temporal variations, and the CGI_i^c based responses bank that includes user-defined thresholds under different crack lengths can be created for crack mapping. Refer to figures 8 and 9 in section 4 for the results of the crack monitoring algorithm.

3. Methodology

This section presents the experimental methodology used in this study. First, the damage law and the numerical model are described. Second, the fatigue loading protocols implemented in FEM are presented. Third, the experimental setup along with the procedure used to investigated the sensor's signal are presented.

3.1. Damage law

The Paris-Erdogan law [35] is a well-utilized power model for characterizing and evaluating fatigue crack propagation (FCP) rate. By considering the crack closure effect and the influence of welding residual stress, the FCP rate can be described as [36]:

$$\left[\frac{da}{dN}\right]_{R_{\mathrm{eff}}>0} = \left(\frac{U_{R_{\mathrm{eff}}>0}}{U_{R_{\mathrm{eff}}=0}}\right)^m \cdot C(\Delta K_{\mathrm{eff}})^m = \left(\frac{U_{R_{\mathrm{eff}}>0}}{U_{R_{\mathrm{eff}}=0}}\right)^m \cdot C(U_{R_{\mathrm{eff}}=0} \cdot \Delta K)^m \quad (19)$$

where C and m are Paris' constants, and ΔK_{eff} is the effective stress intensity factor range defined as:

$$\Delta K_{\mathrm{eff}} = U\Delta K = U(K_{I\max} - K_{I\min}) \quad (20)$$

where U represents stress range ratio, taken as, for structural steel: [37]:

$$U = 0.722 + 0.278\, R_{eff} \quad (21)$$

where R_{eff} is the effective stress ratio characterized by the stress intensity factors (e.g. $K_I$max and $K_I$max) and changes due to the presence of welding residual stress under cyclic load. The stress intensity range ΔK ($K_I\max - K_I\min$) can be computed by using the equation defined in ASTM E2899-19e1 [38]:

$$\Delta K = K_{I\max} - K_{I\min} = (H\sigma_b F_b)\left(\frac{\pi a}{1 + 1.464(\frac{a}{c})^{1.65}}\right)^{1/2} \quad (22)$$

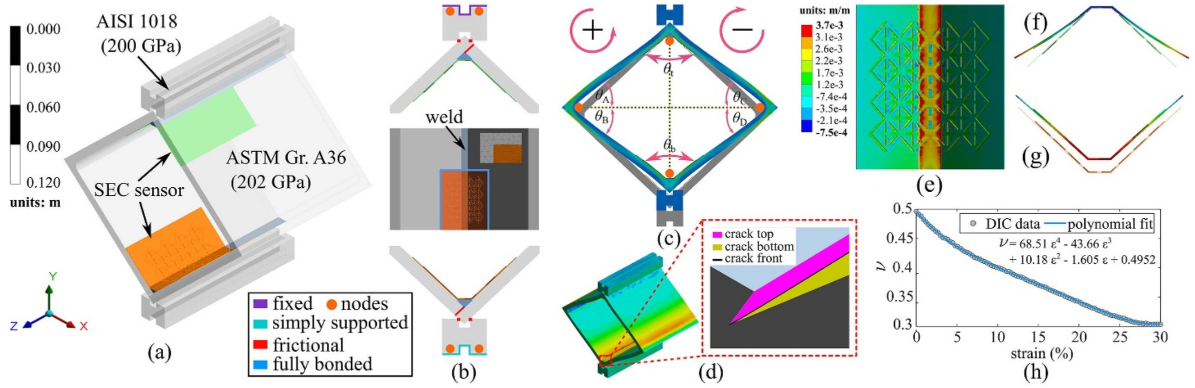

Figure 4. Schematic drawing of the numerical model showing: (a) general geometry of the welded specimen; (b) boundary conditions, meshing style, and mesh element distribution of the cSEC and of the welded specimen; (c) simulated deformation and angular rotation of the welded specimen under compression; (d) simulated maximum principal stress distribution of the welded specimen with a close-up view showing fatigue crack growth and nodes used for the extraction of synthetic measurements; (e) simulated normal elastic strain distribution in the cSEC within a folded configuration; (f) and (g) front section views of the sensor installed at the top (f) and bottom (g) of the cross-section showing the deformation under angular motion; and (h) strain-dependent nonlinear transverse Poisson's ratio of SEBS.

where H and F_b are the combinations of correction factors, σ_b is the bending stress, a is the surface crack depth, and c is the half surface crack length.

3.2. Numerical model

A three-dimensional nonlinear FEM was created in ANSYS 2021 R1 [39] to numerically verify the loading protocol and validate the fatigue behavior obtained experimentally. To mimic a connection of plate-to-web welds in bridges, two 127 mm × 127 mm × 3.175 mm (L5 × 5 × 5/16) steel angles were assembled as a square box by using a three-pass horizontal fillet weld at the top (12 o'clock) and bottom (6 o'clock) of the box, as shown in figure 4(a). The L-shape channels are made from ASTM grade A36 steel, and its geometry is defined in figure 6(d). Because the geometry of a fillet weld is difficult to be modeled precisely as local discontinuities in the fabrication process and irregular sharp surface may exist, the fillet weld is modeled as a prism element as done in other studies [40–43]. Here, prisms of base length 10 mm, side length 8.51 mm, and depth 152.4 mm are added at the top and bottom corners of the box in the FEM, shown in figure 4(a). The cSECs were modeled as corrugate films with a substrate layer thickness of 0.3 mm and a texture height of 0.35 mm, and the SEBS material used for cSEC fabrication was defined as an isotropic polymer with a tensile test-obtained Young's modulus E of 0.41 MPa and a digital image correlation-obtained strain-dependent nonlinear Poisson's ratio ν [29], plotted in figure 4(h). A pair of customized H-shaped fixtures made of AISI 1018 steel are used to support and fix the welded specimen at the edges of the welded corners at the top and bottom of the samples, enabling free angular rotations and an in-depth inner side-to-exterior side crack propagation under fatigue load. The material properties of the AISI 1018 steel, ASTM grade A36 steel, and fillet weld used in the FEM for simulating fatigue crack damage are tabulated in table 1, where the properties of the fillet weld are taken from [44].

A regular-shaped and uniform-sized mesh is used to capture the peak stress at the weld toe and the steep stress gradient around the weld region. The fillet welds are meshed using the quadrilateral method with a mesh size of 0.15 mm with a refined mesh applied to its surrounding area, generating a total of 4302 and 4409 mesh elements on the welds at the top and bottom, respectively. As shown in the onset of figure 4(b), the sensors and the steel specimens along with the fixtures were meshed using the multizone and tetrahedron mesh method with a mesh size of 0.2 and 0.5 mm, respectively. The boundary conditions of the specimen in the numerical simulations are presented in figure 4(b). The prisms are assigned as fully bonded on the angles of the two L-shape channels to mimic weld bonds, and the cSECs were also modeled as fully bonded over the surface of fillet welds as well as the inner surface of the L-shape channels to mimic a full adhesion of the epoxy layer. Consistent with the experimental procedure, contact elements were used by assigning both H-shape fixtures as friction contacts at the interface with a friction coefficient of the contact surfaces taken as 0.78 [45]. The entire specimen was constrained as fixed along the x, y, and z translational degrees-of-freedom (UX, UY, and UZ) at the top of the upper H-shape fixture and constrained as simply supported along the x and z translational degrees-of-freedom (UX and UZ only) at the lower bottom H-shape fixture.

Figure 4(c) presents the simulated deformation and angular rotation of the welded specimen under compression. Figure 4(d) shows the simulated maximum principal stress distributed on the welded specimen, where it can be observed that high stress is concentrated along the edge of the welds consistent with the crack propagation path. The fatigue behavior in the numerical simulation is dominated by Paris' law, and the simulation of the fatigue crack growth behavior on the welded specimen was conducted by following the same procedure used in prior work [30], where the separating morphing and adaptive re-meshing technology crack growth simulation tool was used, and 40 face nodes were uniformly assigned on the top and bottom crack faces, as presented in the onset

Table 1. Assigned properties for AISI 1018 and ASTM grade A36 (Gr. A36) steel, along with the properties of fillet welds.

Material property	AISI 1018	Gr. A36	Fillet welds
Density	7870 kg m^{-3}	7850 kg m^{-3}	7800 kg m^{-3}
Young's modulus	2.00×10^{11} Pa	2.02×10^{11} Pa	7.72×10^{10} Pa
Poisson's ratio	0.29	0.32	0.31
Bulk modulus	1.59×10^{11} Pa	1.67×10^{11} Pa	1.58×10^{11} Pa
Shear modulus	7.80×10^{10} Pa	7.69×10^{10} Pa	8.02×10^{10} Pa
Strength coefficient	—	9.20×10^{8} Pa	—
Strength exponent	—	−0.106	—
Ductility coefficient	—	0.213	—
Ductility exponent	—	−0.47	—
Cyclic strength coefficient	—	1.01×10^{9} Pa	—
Cyclic strain hardening exponent	—	0.2	—
Tensile yield strength	3.70×10^{8} Pa	4.20×10^{8} Pa	3.15×10^{8} Pa
Tensile ultimate strength	4.40×10^{8} Pa	5.60×10^{8} Pa	4.25×10^{8} Pa
Material coefficient C	—	8.13×10^{-11}	—
Exponent m	—	2.81	—

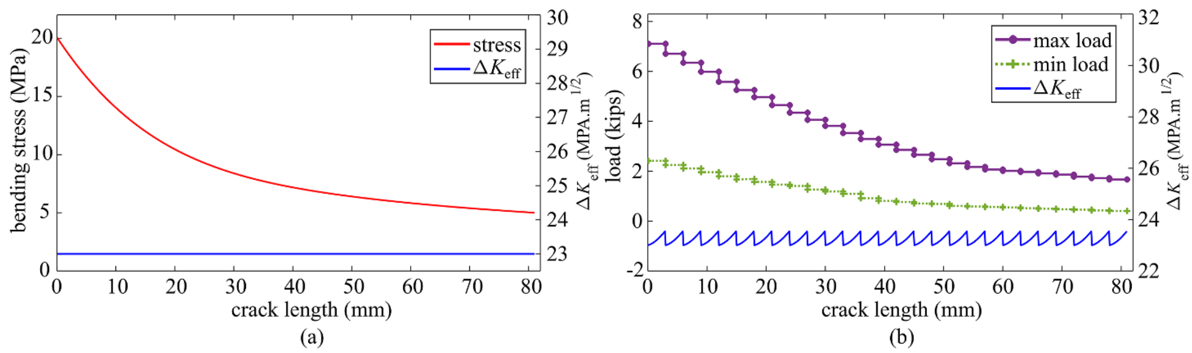

Figure 5. (a) Computed bending stress as a function of crack length on fillet welds; and (b) fatigue loading protocols characterized from FEM.

of figure 4(d), to extract displacements for computing crack-induced strain. Refer to section 4 for the Paris' coefficients C and m used in this simulation. Finally, a split line offset is added onto the welded edges of the welded area to ensure that the nodes are inside the welds and not shared by multiple bodies, as shown in figure 4(d).

Figure 4(e) presents the normal elastic strain distribution on the cSEC installed at the bottom corner, while figures 4(f) and (g) are the front section views of the sensor installed in the top and bottom corners showing the deformation of the sensors under angular motion. The cSEC's signal can be simulated by extracting the initial area $A_0^{p,q}$ and the area after deformation $A^{p,q}$ of each mesh element from the FEM to compute the deformed area $\Delta A^{p,q}$, and substituting them into the FE based algorithm (equation (17)) to obtained the numerical capacitance response.

3.3. Fatigue loading protocol

A value of 23 MPa$\sqrt{m}$ was selected for ΔK as the target stress intensity during the entire crack propagation process, consistent with ASTM E2899-19e1 requirements. An initial crack aspect ratio a/c of 0.1 [46] and residual stress induced effective stress ratio R_{eff} of 0.05, calculated using the procedure reported in [47], were selected to computed the stress range σ_b under different crack lengths through equations (19)–(22). Results are plotted in figure 5(a).

Equation (22) implied that the bending stress σ_b can be determined once a selected ΔK is introduced, with a longer crack length c yielding a larger ΔK if σ_b is fixed. Therefore, the fatigue loading dominated by the designed bending stress σ_b is obtained from the constructed FEM by creating a crack growth path along the edge of the fillet weld to extract bending stresses, as shown in figure 7(a). The results extracted along the defined path under a 0.1 mm crack are plotted in figure 7(b) with the red line representing the average value along the path. It can be observed that approximately 40% higher stress is concentrated at both two ends of the fillet weld under compression, which corresponds to the position of the fatigue crack initiation observed during the experiments.

A stress ratio $R = \sigma_{\mathrm{min}}/\sigma_{\mathrm{max}}$ of 0.3 was selected and used to represent the ratio of live load-induced stress (i.e. vehicle load) to the dead load-induced stress (i.e. bridge self-weight) over one load cycle [48]. Values for F_{max} and F_{min} can be obtained from the numerical model by taking the average values of the yielded bending stress on the defined crack path equal to the calculated bending stress (shown in figure 5(a)). A multistage loading protocol was established in which F_{max}

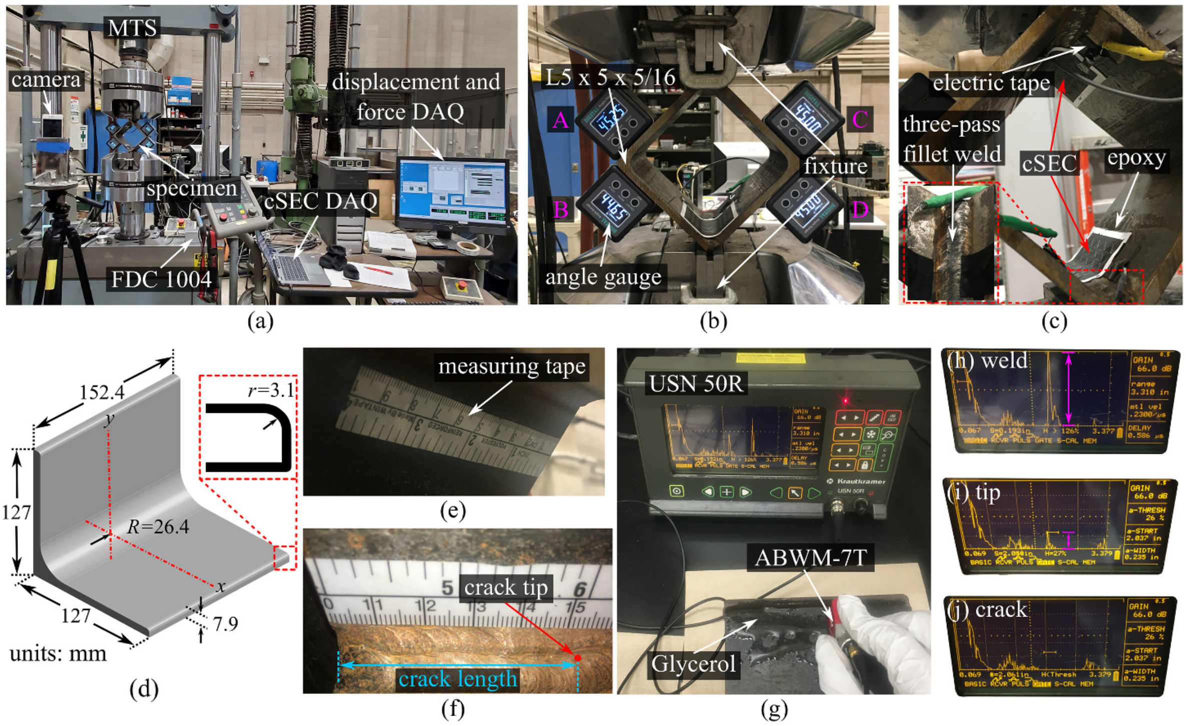

Figure 6. (a) Overall experimental configuration (the arrow indicates the loading direction); (b) zoom on the front side of the welded specimen showing the digital angle gauges and custom H-shape fixture; (c) zoom on the back side of the welded specimen showing cSECs with the onset showing the detail of three-pass fillet weld; (d) geometric configuration of the L5 × 5 × 5/16 L-shaped channel; (e) measuring tape adhered next to the welded at the top corner of specimen 0; (f) picture of a fatigue crack propagated over 52.1 mm; (g) experimental setup for UT testing; and pictures of transmission pulse and defect echo under (h) weld; (i) crack tip; and (h) crack.

and $F_{\min}$ remain constant during each crack interval and are re-computed and adjusted at every 3 mm (0.12 inch) of crack growth, maintaining an approximately constant stress intensity ΔK_{eff} within a range of 23 MPa$\sqrt{m}$ to 23.6 MPa$\sqrt{m}$, as plotted in figure 5(b).

3.4. Experimental procedure

The sensing properties of cSEC under angular rotation-induced bending strain were characterized on a hollow steel section (HSS) (i.e. no weld) in [31]. Here, work is extended by creating the HSS by joining two L-shaped sections via a fillet web. The fillet weld is selected in this study because it provides high shear strength and is typically applied to join two pieces of metal perpendicularly with small joint preparation required [49], and the test setup can be used to mimic a plate-to-web orthogonal weld connection. Four specimens were constructed (numbered 0–3), equipped with the cSEC, and tested under the developed fatigue load protocol. The objectives of the experiments are to characterize the capacitance response and evaluate the performance of the sensor at detecting and quantifying cracks on fillet welds. Figure 6(a) is an annotated picture of the overall experimental configuration.

Figure 6(b) is a close-up view of the front side of a welded specimen. It is fabricated using three-pass horizontal fillet welds along the edges of the two A36 L5 × 5 × 5/16 L-shaped channels. Values of $\varphi = 89.95°$ and $\varphi = 90.05°$, and $d = 11.3$ mm and $d = 11.2$ mm were measured at the corners in the top and bottom corners (figure 6(d)). The inner surface of the welded specimen was sanded using 500 and 1000 grit sandpaper successively and rinsed with acetone to obtain a smooth and clean sensing area. As observable in figure 6(c), the off-the-shelf bi-component epoxy (JB Weld) was applied as a thin layer onto the sanded surface of the fillet welds and cSECs were glued in folded configurations by adhering their flat surface onto the epoxy layer, with each cSEC aligned with an end of the weld and fully adhered onto the welded surface. Electrical tapes were used to affix the wires to minimize signal noise caused by cable movement. Unlike specimens 1–3, specimen 0 only had one cSEC installed over the bottom corner. Specimen 0 was used exclusively to validate the ultrasonic (UT) testing procedure.

Shown in figure 6(e), a peel-and-stick measuring tape with 1 mm marks was adhered next to the crack path along the top corner of specimen 0 to assist a computer-aided visual measurement of the crack length during testing. Figure 6(f) is a photograph of a fatigue crack propagating over 52.1 mm on specimen 0, taken at cycle #50293, with the crack tip indicated by a red dot. Two customized H-shape fixtures fabricated using three AISI 1018 steel plates were placed over the upper and lower edges of the specimen and affixed onto the servo-hydraulic testing machine (MTS model 312.41 with a TestStar IIm controller) grips. To measure localized angular rotations along the top (θ_t) and bottom (θ_b) directions, four digital angle gauges, identified as A, B, C, and D in figure 6(b), were installed above and below the left and right corners. Those digital angle gauges have a minimum measurable degree resolution of 0.05° with a minimum reaction time of 0.1 s. These rotations correspond to the real angular rotation experienced by the installed cSEC sensors, with $\Delta\theta_t = |\Delta\theta_A| + |\Delta\theta_C|$ and $\Delta\theta_b = |\Delta\theta_B| + |\Delta\theta_D|$. The measurements from each angle gauge could also be obtained from the numerical model. They were assigned as negative for clockwise rotations and positive for counterclockwise rotations, as indicated in figure 4(c).

A preload of 0.05 kN was applied on the welded specimen prior to each test for a compression-compression mode. A loading frequency of 2 Hz was selected for initiating and propagating fatigue cracks. For simultaneously recording the rotated angular degrees, a digital camera with a frame rate of 30 fps was placed in front of the specimen to record the measurements from the angle gauges. Capacitance data collection was performed using a custom DAQ at a sampling frequency of 80 samples/second in the LabVIEW environment, and load and displacement data were recorded from the LVDT of the MTS at 20 samples s^{-1}.

UT testing was performed using a Krautkramer Branson USN-50 R ultrasonic flaw detector equipped with an ABWM-7 T-60 wedge probe to detect and quantify crack lengths under the sensor. The UT setup, shown in figure 6(g), used non-toxic Glycerin with an acoustic impedance of 2.42 kg/m^{-12}s $\times 10^6$ uniformly applied onto the exterior surface of the fillet welds to provide good contact and facilitate the transmission of sound waves. The ultrasonic flaw detector was set with a gain of 66 dB, displacement range of 84.07 mm (3.31 inch), sound velocity of 5 918 200 mm s^{-1} (0.233 inch μs^{-1}), and probe delay of 0.586 µs. The crack condition was identified by observing the transmission pulse and defect echo, where a significant amplitude, reduction in amplitude, and disappearance of amplitudes correspond to a weld, a crack tip, and a crack, respectively, as shown in figures 6(h)–(i).

4. Results and discussion

This section analyzes experimental data to validate the methodology, including the numerical model, UT tests, and FEM, and then examines the performance of the cSEC at monitoring cracks in fillet welds.

4.1. Damage model validation

Figure 7(c) plots the experimental S-N curves along with a linear interpolation to represent the crack propagation rates in terms of da/dN (increment of crack length per load cycle). Values for da/dN ranges from da/dN = 1.88×10^{-8} (m/cycle) to maximum da/dN = 6.49×10^{-7} (m/cycle) over the three specimens. These values are consistent with those reported in literature as typical in FCP [50].

Figure 7(c) is a plot showing the variation in the fatigue crack length. It can be observed that the propagation rate varies with the fatigue load, implying a variability in the Paris' coefficients C and m over each crack growth interval. Figure 7(d) shows the crack growth rate (da/dN) as a function of stress intensity range (ΔK) in a log scale plot, where data is taken from the crack growth interval 9.09–12.06 mm on specimen 1. To quantify C and m in this selected interval, regime B was first identified on the curve by computing the threshold values of K_1 and K_2 following the threshold equation defined in [51], represented by green dashed lines. After, a linear regression (red dashed line) was applied on regime B, and the Paris' coefficient C and exponent m were respectively taken as intercept on y-axis and determined as the slope of the fitted line [52].

The Paris' coefficients C and m throughout the test were characterized on each crack interval following the same procedure, and results are tabulated in tables 2 and 3, where the superscripts b and t denote the 'bottom' and 'top' corner, respectively. The 'range' is the resulting range of the coefficients found on each interval for specimen 1, and 'range*' is the same range but over specimens 1–3. Overall, the ranges of both Paris's coefficients C and m found in those experimental tests are all in the valid ranges reported in [50, 53].

4.2. UT validation

Figure 7(e) is a plot of crack length versus the number of cycles comparing measurements from UT and from the computer-aided visual approach at the top corner of specimen 0. Visualized crack lengths were obtained via photographs taken during the test, and post-processed with PHOTOSHOP for resolution enhancement and measured by the image processing software IMAGEJ. A mean absolute percentage error (MAPE) of 4.03% was obtained between both measurement methods, indicating a good agreement. This validates the UT procedure for the detection and quantification of crack lengths on specimens 1–3, where the crack is covered by the sensors.

4.3. Numerical model validation

Validation of the numerical model is conducted using experimental data to examine the accuracy of the modeling assumptions. First, the fatigue crack growth behavior using the experimentally obtained Paris' coefficients C_i and m_i was investigated. Figure 8(a) presented crack lengths as a function of the number of cycles at both the top and bottom corners. Fatigue cracks were simulated using all sets of C_i and m_i found experimentally (table 2), with results presented as a range (shaded area in figure 8(a)) Parameters $C_i^{\mathrm{t}} = 8.13 \times 10^{-11}$, $m_i^{\mathrm{t}} = 2.81$ and $C_i^{\mathrm{t}} = 5.08 \times 10^{-11}$, $m_i^{\mathrm{t}} = 2.71$ found from the 15.11 to 18.09 mm and 6.31 to 8.39 mm crack intervals at the top and bottom corners of specimen 1 were used for the numerical simulations. Results, plotted in the figure with solid lines, are all within the ranges.

Second, the mechanical properties of the welded specimen were validated by comparing the generated maximum displacements under different crack lengths. Experimental and numerical data are extracted from the LVDT of the MTS and the created nodes in the FEM (shown in figure 4(c)), respectively, are plotted in figure 8(b). There is a good agreement between both datasets, with a maximum fitting error of 4.9%.

Third, the deflective shape of the welded specimen under compression is investigated by quantifying rotated angular degrees ($\Delta\theta_i$) under different crack lengths. Results are plotted

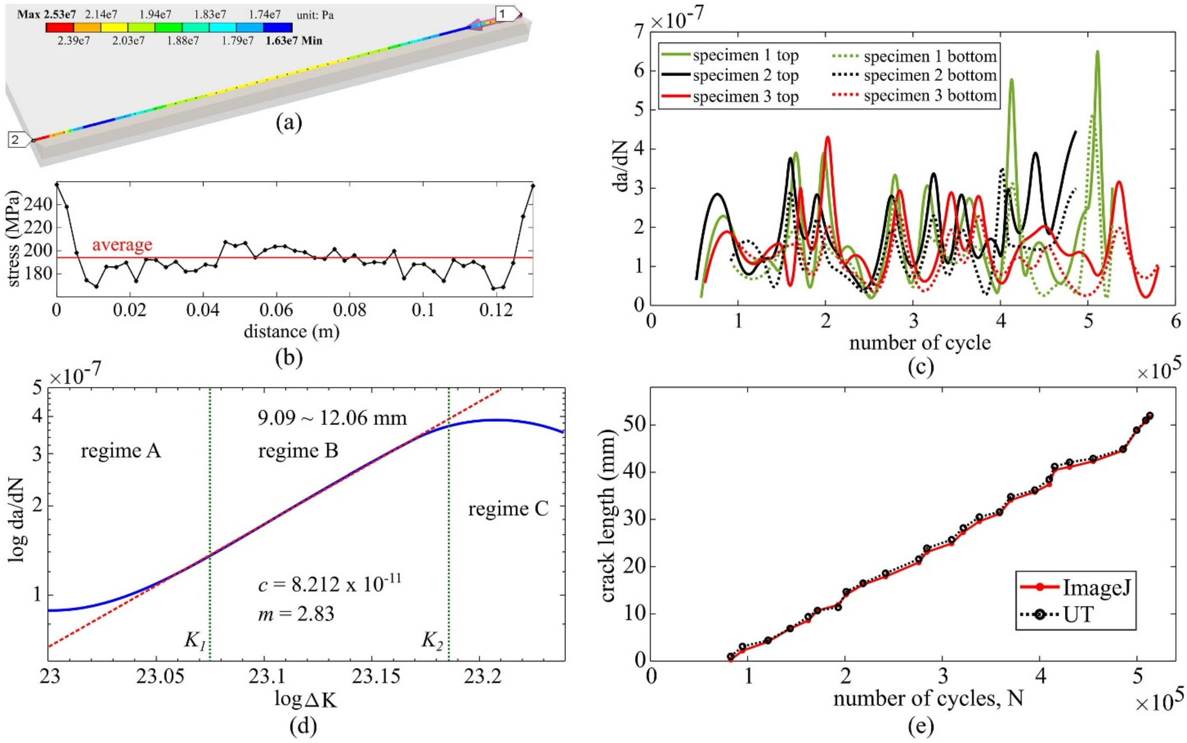

Figure 7. (a) Defined crack path along with the distribution of simulated bending stress along the path; (b) extracted bending stress values along the crack path; (c) crack growth rate (da/dN) as a function of loading cycles; (d) typical crack growth rate with respect to the stress intensity range in log scale; and (e) comparison of the visualized crack lengths with their results detected from UT.

Table 2. Experimentally obtained Paris' coefficients computed under different crack length intervals at the top (^{t}) and bottom (^{b}) corners.

Top crack length (mm)	0–2	2–4	…	48–50	Range	Range*
C_i^{t}	3.55×10^{-11}	4.63×10^{-11}	…	9.02×10^{-11}	2.801×10^{-11}–1.003×10^{-10}	$2.66 \times 10^{-11}-1.001 \times 10^{-10}$
m_i^{t}	2.68	2.72	…	2.70	2.64–2.71	2.65–2.76

Table 3. Experimentally obtained Paris' coefficients computed under different crack length intervals at the top (^{t}) and bottom (^{b}) corners.

Top crack length (mm)	0–3	3–6	…	78–81	Range	Range*
C_i^{b}	7.21×10^{-11}	1.12×10^{-10}	…	1.52×10^{-10}	6.708×10^{-11}–1.601×10^{-10}	6.13×10^{-11}–1.552×10^{-10}
m_i^{b}	2.83	2.81	…	2.85	2.69–2.85	2.68–2.88

in figure 8(c) as a function of crack length at both the top and bottom corners for all three specimens, where the FEM outputs are extracted from the nodes located at the corners and compared against those obtained from laboratory experiments (measured from the digital angle gauges). Numerical results exhibited a good match of the experimental data with a MAPE of 4.39% and 6.08% at the top and bottom corners, respectively. The rotated angular degrees measured at the top corner ($|\Delta\theta_A| + |\Delta\theta_C|$) are found to be consistently lower than those measured at the bottom corner ($|\Delta\theta_B| + |\Delta\theta_D|$), which can be explained by the asymmetric boundary conditions of the experimental setup.

Fourth, the electromechanical model (equation (10)) is validated by comparing the numerical capacitance response ($\Delta C/C_0$) to the experimentally measured capacitance. Figure 8(d) is a typical time series plot of the raw data measured from the cSEC (installed at the bottom corner of specimen 1) compared against the numerical response under a crack length of 9.1 mm. The measured angular rotations $\Delta\theta_B$ and $\Delta\theta_D$ were substituted into equation (15) for α and β to convert angular rotations into bending strain $\varepsilon_{x,c}$, represented by the blue line in figure 8(d), and the numerical capacitance response was estimated by using equation (10) with the computed bending strain $\epsilon_{x,c}$. A good fit between the experimental and numerical results in both the magnitude and phase of the capacitance response was found, with a root mean square error (RMSE) of 5.53%. The fitting errors can be explained by modeling assumptions in the electromechanical model, such as the approximation of the fillet weld as a curved surface.

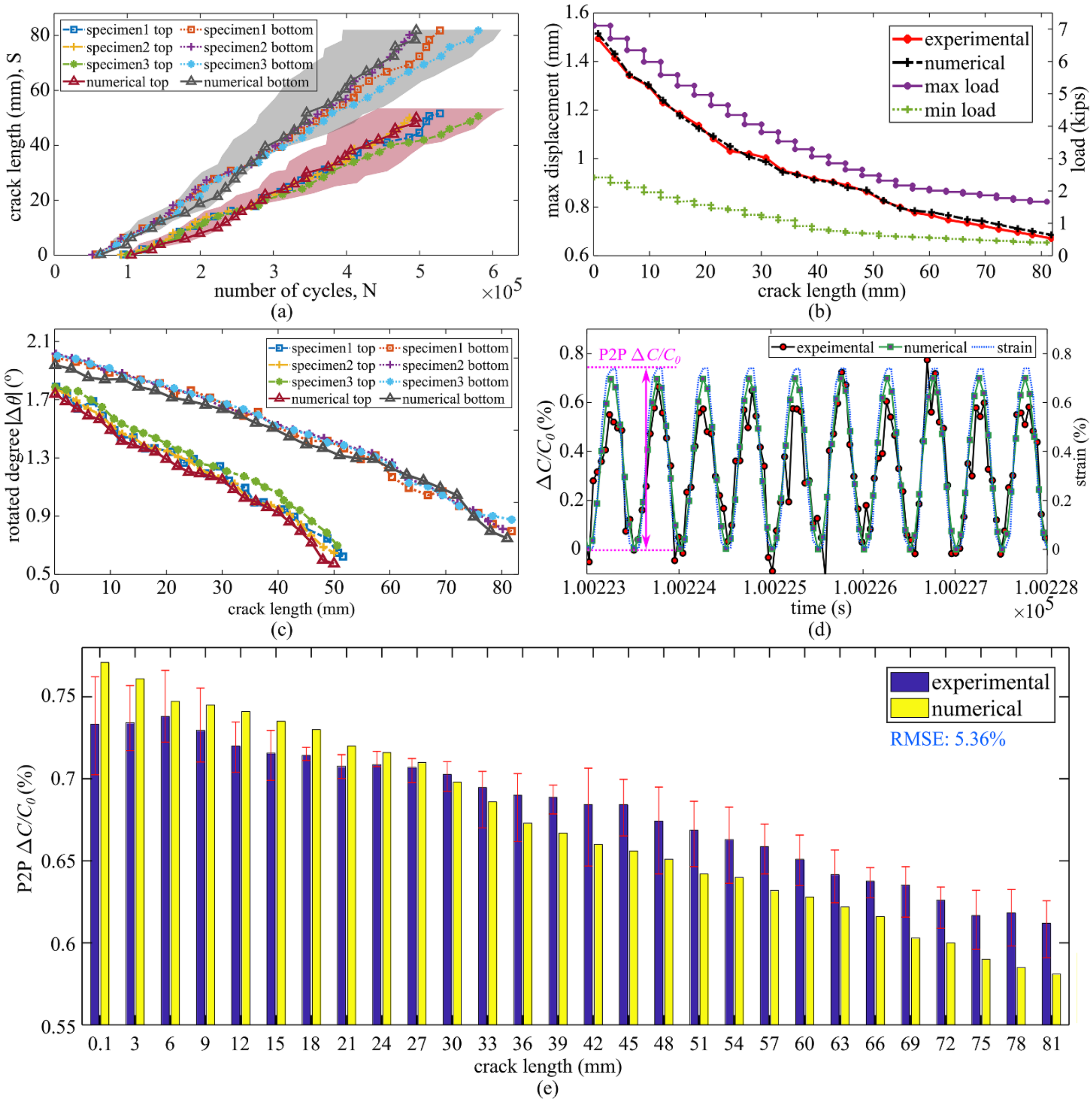

Figure 8. Comparison of numerical and experimental data: (a) crack lengths as a function of the number of cycles over specimens 1–3; (b) averaged maximum displacements under each crack interval; (c) rotated angular degree as a function of crack length over specimens 1–3; (d) measured time series signals of capacitance response $\Delta C/C_0$ under a crack length of 9.1 mm; and (e) average P2P $\Delta C/C_0$ amplitudes as a function of the crack length with the error bars indicating the min–max ranges.

Finally, the averaged numerical and experimental P2P $\Delta C/C_0$ (figure 8(d)) amplitudes are compared. Figure 8(e) is a bar chart comparing results, with the error bars indicating the min–max range of the P2P amplitudes measured over the three specimens. It can be found that the numerical P2P amplitudes are closely matching with the experimental, with an RMSE of 5.36% and a maximum difference of 8.91% found under the 42 mm crack length. At a glance, experimental results (i.e. crack response) show less sensitivity (slope of the bar chart) to the crack length than numerical ones, as shown in figure 8(e). Discrepancies can be attributable to the unmodeled capacitance response arising from the out-of-plane strain and the irregular surface of the fillet weld.

4.4. Crack monitoring performance

4.4.1. CGI (CGI_i^c). The PSD amplitudes are extracted from the signals over different crack lengths, which represent the magnitude of the dominating frequency peak. Figure 9(a) plots the PSD^m amplitudes (from the cSEC signals) as the function of crack lengths. One can observe that the PSD^m amplitudes decrease with increasing crack length, attributable to the reduction in bending strain from the reduction in the compression load.

To filter bending strain-induced capacitance response from the measured signal and eliminate the effect of the angular rotation, two linear regressions following findings in [31]

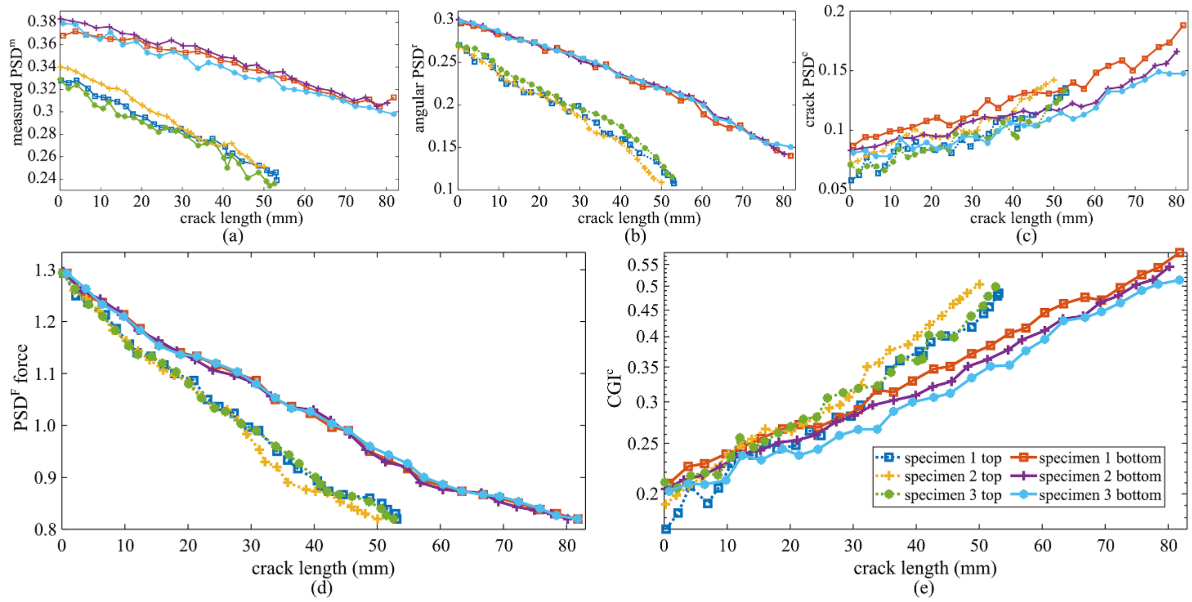

Figure 9. Signal study conducted in the top and bottom directions over three specimens: (a) measured; (b) angular rotation induced; and (c) crack induced P2P amplitudes of the relative change in capacitance $\Delta C/C_0$ as a function of crack lengths; (d) measured; (e) angular rotation induced; and (f) crack induced PSD amplitudes of measured time series data in capacitance response as a function of crack lengths; (g) PSD amplitudes of measured time series data in compression load under different crack lengths; and (h) semi-log plot of crack induced CGI^c as a function of the crack length.

are used to identify the part of the signal caused by bending strain, which in turn can be used to identify angular rotation-induced amplitudes $\mathrm{PSD}^{\mathrm{r}}$ using equation (15) (with $\Delta\theta_i$ shown in figure 8(c)). Results for the $\mathrm{PSD}^{\mathrm{r}}$ under each crack length are plotted in figure 9(b), also exhibiting an inverse relationship with crack length due to the reduction in the compression load.

After, the crack-induced amplitudes PSD^c are obtained by subtracting $\mathrm{PSD}^{\mathrm{r}}$ (figure 9(b)) $\mathrm{PSD}^{\mathrm{m}}$ (figure 9(a)), and results are plotted in figure 9(c). It can be noticed that the PSD^c are positive and approximately linear with respect to crack length, as desired.

Lastly, the CGI is constructed using equation $\frac{\sqrt{\mathrm{PSD}_i^c}}{\sqrt{\mathrm{PSD}_i^{\mathrm{F}}}}$. Figure 9(g) plots the $\mathrm{PSD}^{\mathrm{F}}$ amplitudes of loading input under each crack length, and figure 9(h) presents results in term of CGI^c as a function of crack length in a semilog scale plot, where the superscript c denotes 'crack-induced' where PSD^c (figure 9(c)) was used the computation. A positive and approximately linear relationship between the CGI_i^c and the crack length is observed on the signal measured from all of the six installed cSECs, with the linear fit yielding R^2 values between 0.909 and 0.943. The produced values of the coefficient R^2 demonstrate high linearity and thus show considerable potential for using CGI_i^c as an actionable metric for fatigue crack mapping on fillet welds.

4.4.2. Crack monitoring algorithm. The signal is further processed using the proposed crack monitoring algorithm (figure 3) to validate and verify the capability of a given sensor at discovering and quantifying fatigue cracks. The discovery of a fatigue crack is achieved by conducting a continuous paired t-test on and CGI_i^c. To do so, the time-series signal of both the capacitance and loading force signals were split into numerous windows with each window covering a 100-second dataset, and each 100-second dataset was further split evenly into ten 10-second datasets, named as a 'subsets'. The data in each subset were extracted and converted to the frequency domain to obtain CGI_i^c amplitudes.

Thus, ten values of the CGI_i^c are included in each 100-second window. To eliminate early-stage chattering in the signal, data in the first two windows was discarded, and the third window (time interval 201–300 s) was taken as the reference window. A continuous paired t-test was conducted on the CGI_i^c by using the TTEST function in MATLAB, and the test is under the null hypothesis that the mean of the 10 CGI_i^c values in a new window is the same as those in the reference window. Figure 10(a) presents the averaged value of CGI_i^c in each window in the form of a time series, obtained from the bottom corner of specimen 1, and figure 10(b) presents resulting p-values computed from each window. It can be observed that the p-values stabilized to 1 after the 382nd windows, which indicates that the t-test rejects the null hypothesis with a 5% significance level, and therefore that a crack is detected.

Table 4 lists and compares results for the CGI_i^c in terms of the detected number of windows, corresponding time interval, corresponding number of cycles, and resulting crack lengths found by applying the crack monitoring algorithm to the signal taken from each sensor installed over the specimen 1–3. The crack lengths are obtained from the validated numerical model by inputting the number of cycles. It can be observed that the minimum detectable crack length ranges from 0.48 to 0.61 mm, which are slightly longer than the 0.31 mm reported in prior work on the cSEC for when detecting fatigue

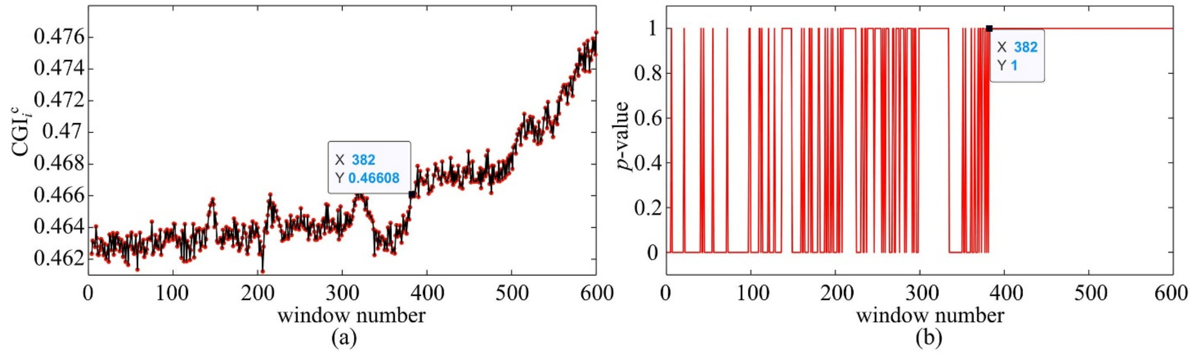

Figure 10. (a) Time series of averaged CGI_i^c values taken from each window; and (b) the computed p-value for the first 60 000 s of the signal.

Table 4. Experimental results obtained from the crack monitoring algorithm.

		Top corner				Bottom corner			
	Sample	Window (#)	Time interval (s)	Cycle (#)	Crack length (mm)	Window (#)	Time interval (s)	Cycle (#)	Crack length (mm)
CGI	1	515	51 800–51 900	103 600–103 800	0.48	382	38 500–38 600	77 000–77 200	0.59
	2	530	53 300–53 400	106 600–106 800	0.50	361	36 400–36 500	72 600–72 700	0.52
	3	518	52 100–52 200	104 200–104 400	0.49	390	39 300–39 400	78 600–78 800	0.61

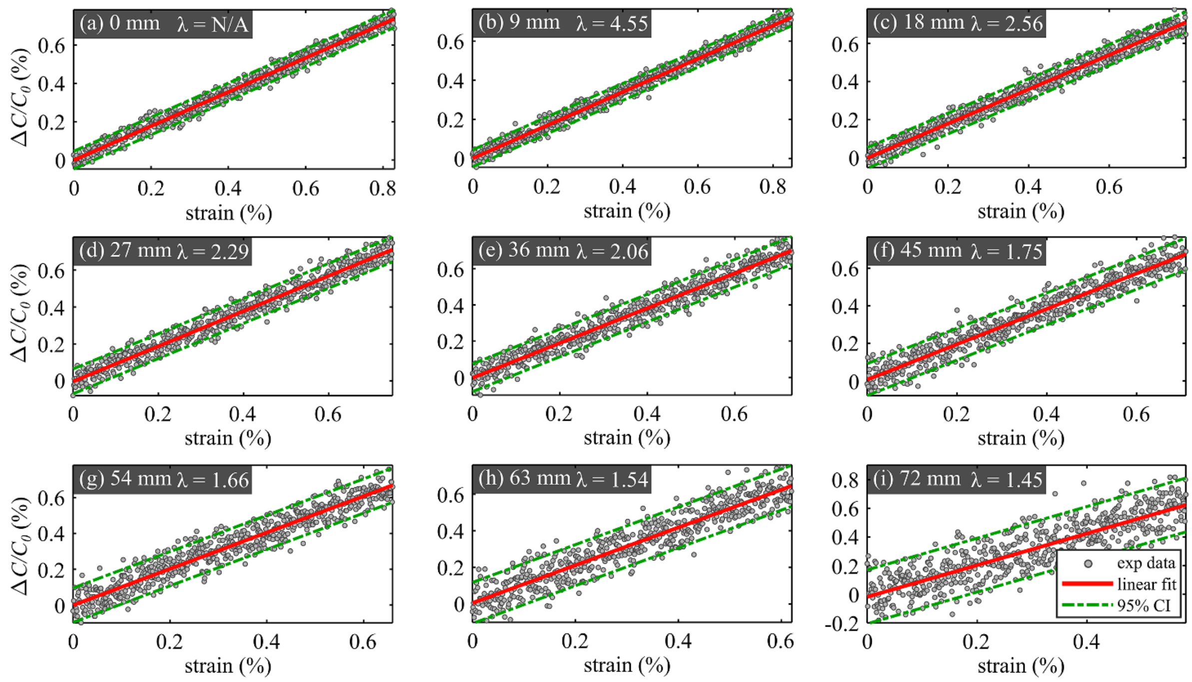

Figure 11. Three-specimen averaged relative change in capacitance ($\Delta C/C_0$) as a function of the MTS-derived strain under crack lengths of (a) 0 (undamaged); (b) 9; (c) 18; (d) 27; (e) 36; (f) 45; (g) 54; (h) 63; and (i) 72 mm.

cracks over the flat surface of a compact tension (C(T)) specimen, attributable to the more complex geometry under consideration.

4.4.3. Overall sensing performance. Figure 11 plots the relative change in capacitance $\Delta C/C_0$ as a function of the MTS-derived strain (strain computed from MTS displacement) under crack lengths of 0, 9, 18, 27, 36, 45, 54, 63, and 72 mm. Values of the MTS-derived strain are extracted from the LVDT under the corresponding load and crack lengths, and the plots show the averaged measurements from specimens 1–3 installed at the bottom corners, along with a linear fit (red solid line) conducted within a 95% confidence interval (CI) bound (dashed green lines). The gauge factors, corresponding to the slopes of the linear fits, are shown in each subplot.

Table 5. Experimental results characterizing sensing performance.

Crack length (mm)	MTS-derived strain (%)	Crack strain (%)	Bending strain (%)	Strain ratio (%)	R^2 (−)	Crack λ (−)	95% CI $\Delta C/C_0$ (−)	95% CI resolution (με)	σ_{res} (με)
0	0.83	0.01	0.82	1.22	0.94	N/A	±0.049	—	—
9	0.85	0.16	0.69	23.19	0.95	4.55	±0.041	±9.1	6.31
18	0.79	0.28	0.51	54.91	0.90	2.56	±0.055	±21.5	9.52
27	0.75	0.31	0.44	70.46	0.86	2.29	±0.065	±28.4	8.33
36	0.73	0.34	0.39	87.18	0.83	2.06	±0.076	±36.9	10.08
45	0.71	0.38	0.33	151.15	0.81	1.75	±0.088	±50.3	13.93
54	0.66	0.39	0.27	144.44	0.77	1.66	±0.103	±62.1	20.42
63	0.62	0.41	0.21	195.23	0.76	1.54	±0.113	±73.4	29.51
72	0.59	0.43	0.16	268.75	0.71	1.45	±0.201	±138.6	38.45

Table 5 assembles the quantitative results under each crack length, also presented as the averaged values over specimens 1–3, showing the MTS-derived strain, the goodness of linear fit (R^2 value), the gauge factor (sensitivity) λ obtained from the localized crack strain (across-crack strain obtained using the FEM), accuracy (95% fit) in terms of $\Delta C/C_0$, equivalent strain resolution, and standard deviation of the measurements σ_{res}. The equivalent strain resolutions are computed from $\Delta C/C_0$ and the gauge factor λ obtained from the crack strain. Results show that the MTS-derived strain and across-crack strain are respectively decreasing and increasing, resulting in the increase of the strain ratio (the percentage of strain attributable to the crack versus bending) as the crack propagates. The decreasing of the MTS-derived strain can be explained by the reduction of the fatigue loading under a longer crack length.

It can also be observed that the gauge factor decreases with the increase in crack length, attributable to the increase of the crack strain and strain ratio under a longer crack length. The gauge factor value under the 0 mm crack is discarded given the null level of crack strain.

Overall, the cSECs exhibited good performance on linearity (R^2), resolution (95% CI), and accuracy (σ_{res}) under no crack (0 mm crack). As the crack forms and propagates, these metrics degrade, which can be attributed to the assumptions made in the electromechanical model yielding unmodeled kinematics and smaller signal-to-noise (SNR) ratio under smaller actuation levels (smaller MTS-derived strain). The observed decrease of SNR and crack detection sensitivity of LAE under smaller strain levels have been reported in other researches [54].

5. Conclusion

This paper examined the use of an ultra compliant and flexible strain gauge, termed cSEC, to monitor fatigue cracks in corner welds. The study built on prior work investigating the electromechanical behavior of the sensor for measuring angular rotations within a folded configuration (i.e. no weld nor crack). The objective here was to determine if the sensor, when installed in a folded configuration, could detect fatigue cracks, and if its signal could be used to quantify the level of damage.

A FEM was constructed to characterize the fatigue loading protocol and simulate fatigue behavior. Experiments were conducted on a welded steel specimen in a laboratory environment subjected to high-cycle fatigue damage. A three-pass horizontal fillet weld was selected and applied on the edge of two steel angles for welded corners and to mimic behavior at plate-to-web orthogonal connections in steel bridges. The cSEC sensors were fully adhered to the surface of the fillet welds and subjected to angular rotation-induced bending deformation under compression force. A CGI (CGI_i^c) metric was developed to transform the sensor data into actionable information.

Results showed that the overall PSD amplitudes of the measured signal decreased as the crack propagated, but that both the crack-induced PSD amplitudes as well as the crack-induced CGI_i^c showed a positive and approximately linear relationship with respect to crack length. The proposed algorithm demonstrated promise at crack quantification through t-tests conducted on the CGI_i^c, with a minimum detectable crack length of 0.48 mm. Such resolution is adequate for the foreseen application. The cSEC also exhibited a good overall sensing performance, yet with decreasing linearity, resolution, and accuracy with increasing crack length, attributable to the simplification of the electromechanical model and higher noise produced by the loading equipment under smaller applied displacement. Overall, this study demonstrated the promise of the cSEC at detecting and quantifying fatigue cracks in a folded configuration, thus demonstrating that it could be used to monitor fatigue cracks over complex geometries.

Data availability statement

The data that support the findings of this study are available upon reasonable request from the authors.

Funding

This research was funded by the Departments of Transportation of Iowa, Kansas, South Carolina, and North Carolina, through the Transportation Pooled Fund Study TPF-5(449).

Acknowledgments

The authors are grateful to the sponsors for their support; and to Owen Steffens and Andrew Goreczny at the Department of Civil, Construction and Environmental Engineering of Iowa State University for their assistance with experimental tests.

ORCID iDs

Han Liu https://orcid.org/0000-0003-3057-522X
Simon Laflamme https://orcid.org/0000-0002-0601-9664
Jian Li https://orcid.org/0000-0003-3439-7539
Caroline Bennett https://orcid.org/0000-0002-2713-0011
Austin R J Downey https://orcid.org/0000-0002-5524-2416

References

[1] Campbell F C 2012 *Fatigue and Fracture: Understanding the Basics* (Materials Park, OH: ASM Int.)
[2] Haghani R, Al-Emrani M and Heshmati M 2012 Fatigue-prone details in steel bridges *Buildings* **2** 456–76
[3] Dexter J M and Ocel R J 2013 Manual for repair and retrofit of fatigue cracks in steel bridges (United States: Federal Highway Administration)
[4] Connor R J and Lloyd J B 2017 Maintenance actions to address fatigue cracking in steel bridge structures: proposed guidelines and commentary *Technical Report*
[5] Oh S H, Ryu T Y, Park S H, Won M G, Kang S J, Lee K S, Lee S H, Kim M K and Choi J B 2015 Evaluation of J-groove weld residual stress and crack growth rate of PWSCC in reactor pressure vessel closure head *J. Mech. Sci. Technol.* **29** 1225–30
[6] Farmer F M 1921 The desirability of standardization in the testing of welds *Proc. Inst. Mech. Eng.* **100** 225–88
[7] Campbell L E, Connor R J, Whitehead J M and Washer G A 2020 Benchmark for evaluating performance in visual inspection of fatigue cracking in steel bridges *J. Bridge Eng.* **25** 04019128
[8] Campbell L E, Connor R J, Whitehead J M and Washer G A 2020 Human factors affecting visual inspection of fatigue cracking in steel bridges *Struct. Infrastruct. Eng.* **17** 1447–58
[9] Haagensen P J 2013 *IIW Recommendations on Methods for Improving the Fatigue Strength of Welded Joints: IIW-2142-10* (Cambridge, UK, Philadelphia, PA: Woodhead Publ., Int. Institute of Welding)
[10] Sakagami T, Izumi Y, Shiozawa D, Fujimoto T, Mizokami Y and Hanai T 2016 Nondestructive evaluation of fatigue cracks in steel bridges based on thermoelastic stress measurement *Proc. Struct. Integr.* **2** 2132–9
[11] Amiri N, Farrahi G, Kashyzadeh K R and Chizari M 2020 Applications of ultrasonic testing and machine learning methods to predict the static & fatigue behavior of spot-welded joints *J. Manuf. Process.* **52** 26–34
[12] Wu S, Yu C, Yu P, Buffière J, Helfen L and Fu Y 2016 Corner fatigue cracking behavior of hybrid laser AA7020 welds by synchrotron x-ray computed microtomography *Mater. Sci. Eng.* A **651** 604–14
[13] Dong X, Taylor C J and Cootes T F 2021 A random forest-based automatic inspection system for aerospace welds in x-ray images *IEEE Trans. Autom. Sci. Eng.* **18** 2128–41
[14] Zolfaghari A, Zolfaghari A and Kolahan F 2018 Reliability and sensitivity of magnetic particle nondestructive testing in detecting the surface cracks of welded components *Nondestruct. Test. Eval.* **33** 290–300
[15] Gonchar A V, Klyushnikov V A, Mishakin V V and Anosov M S 2021 Ultrasonic and eddy-current fatigue monitoring of austenitic steel welded joints *Russ. J. Nondestruct. Test.* **57** 570–8
[16] Yu J, Ziehl P, Zárate B and Caicedo J 2011 Prediction of fatigue crack growth in steel bridge components using acoustic emission *J. Constructional Steel Res.* **67** 1254–60
[17] Yu J, Ziehl P, Matta F and Pollock A 2013 Acoustic emission detection of fatigue damage in cruciform welded joints *J. Constructional Steel Res.* **86** 85–91
[18] Chai M, Zhang J, Zhang Z, Duan Q and Cheng G 2017 Acoustic emission studies for characterization of fatigue crack growth in 316ln stainless steel and welds *Appl. Acoust.* **126** 101–13
[19] Araromi O A *et al* 2020 Ultra-sensitive and resilient compliant strain gauges for soft machines *Nature* **587** 219–24
[20] Costa J C, Spina F, Lugoda P, Garcia-Garcia L, Roggen D and Münzenrieder N 2019 Flexible sensors—from materials to applications *Technologies* **7** 35
[21] Liao Y, Zhou P, Pan D, min Zhou L and Su Z 2019 An ultra-thin printable nanocomposite sensor network for structural health monitoring *Struct. Health Monit.* **20** 894–903
[22] Wang Y, Qiu L, Luo Y and Ding R 2019 A stretchable and large-scale guided wave sensor network for aircraft smart skin of structural health monitoring *Struct. Health Monit.* **20** 861–76
[23] Chen T, He Y and Du J 2018 A high-sensitivity flexible eddy current array sensor for crack monitoring of welded structures under varying environment *Sensors* **18** 1780
[24] Yan J and Sun Q 2019 Active monitoring of fatigue crack in the weld zone of bogie frames using ultrasonic guided waves *Sensors* **19** 3372
[25] ONO D, Chao-Nan X, Li C and Bu N 2010 Visualization of internal defect of a pipe using mechanoluminescent sensor *J. Japan. Soc. Exp. Mech.* **10** s152–6
[26] Jinachandran S, Ning Y, Wu B, Li H, Xi J, Prusty B G and Rajan G 2020 Cold crack monitoring and localization in welding using fiber bragg grating sensors *IEEE Trans. Instrum. Meas.* **69** 9228–36
[27] Ali L, Khan S, Bashmal S, Iqbal N, Dai W and Bai Y 2021 Fatigue crack monitoring of t-type joints in steel offshore oil and gas jacket platform *Sensors* **21** 3294
[28] Zhang Y, Hao Q, Cai G, Lv J and Yang C 2020 Crack damage identification and localisation on metro train bogie frame in IoT using guided waves *Sensors* **14** 1403–9
[29] Liu H, Yan J, Kollosche M, Bentil S A and Laflamme S 2020 Surface textures for stretchable capacitive strain sensors *Smart Mater. Struct.* **29** 105037
[30] Liu H, Laflamme S, Li J, Bennett C, Collins W, Downey A, Ziehl P and Jo H 2021 Investigation of surface textured sensing skin for fatigue crack localization and quantification *Smart Mater. Struct.* **30** 105030
[31] Liu H, Laflamme S, Li J, Bennett C, Collins W, Downey A, Ziehl P and Jo H 2021 Soft elastomeric capacitor for angular rotation sensing in steel components *Sensors* **21** 7017
[32] Cai L *et al* 2013 Super-stretchable, transparent carbon nanotube-based capacitive strain sensors for human motion detection *Sci. Rep.* **3** 3048
[33] Pasadas F and Jimenez D 2016 Large-signal model of graphene field-effect transistors—part I: compact modeling of GFET intrinsic capacitances *IEEE Trans. Electron Devices* **63** 2936–41

[34] Kong X, Li J, Bennett C, Collins W, Laflamme S and Jo H 2019 Thin-film sensor for fatigue crack sensing and monitoring in steel bridges under varying crack propagation rates and random traffic loads *J. Aerosp. Eng.* **32** 04018116
[35] NEWBY M 1991 Estimation of Paris-Erdogan law parameters and the influence of environmental factors on crack growth *Int. J. Fatigue* **13** 291–301
[36] Gadallah R, Osawa N, Tanaka S and Tsutsumi S 2018 Critical investigation on the influence of welding heat input and welding residual stress on stress intensity factor and fatigue crack propagation *Eng. Fail. Anal.* **89** 200–21
[37] Kumar R 1992 Review on crack closure for constant amplitude loading in fatigue *Eng. Fract. Mech.* **42** 389–400
[38] A E2899-19e1 2019 Standard test method for measurement of initiation toughness in surface cracks under tension and bending (West Conshohocken, PA: ASTM Int.) (available at:www.astm.org)
[39] Ansys® Academic Research Mechanical, Release 18.1 2020 Help system, coupled field analysis guide (ANSYS, Inc.)
[40] Barsoum Z and Lundbäck A 2009 Simplified FE welding simulation of fillet welds – 3D effects on the formation residual stresses *Eng. Fail. Anal.* **16** 2281–9
[41] Krejsa M, Brozovsky J, Mikolasek D, Parenica P, Koubova L and Materna A 2017 Numerical modeling of fillet and butt welds in steel structural elements with verification using experiment *Proc. Eng.* **190** 318–25
[42] Tousignant K and Packer J A 2018 Fillet weld effective lengths in CHS x-connections. II: finite element modelling, parametric study and design *J. Constructional Steel Res.* **141** 77–90
[43] Yang L, Cui Y, Wei X, Li M and Zhang Y 2019 Strength of duplex stainless steel fillet welded connections *J. Constructional Steel Res.* **152** 246–60
[44] Krejsa M, Brozovsky J, Mikolasek D, Parenica P, Flodr J, Materna A, Halama R and Kozak J 2018 Numerical modeling of steel fillet welded joint *Adv. Eng. Softw.* **117** 59–69
[45] Totten G E (ed) 2017 *ASM Handbook Volume 18: Friction, Lubrication and Wear Technology* (Materials Park, OH: ASM Int.)
[46] Mikulski Z and Lassen T 2019 Fatigue crack initiation and subsequent crack growth in fillet welded steel joints *Int. J. Fatigue* **120** 303–18
[47] Servetti G and Zhang X 2009 Predicting fatigue crack growth rate in a welded butt joint: the role of effective r ratio in accounting for residual stress effect *Eng. Fract. Mech.* **76** 1589–602
[48] Kong X, Li J, Collins W, Bennett C, Laflamme S and Jo H 2017 A large-area strain sensing technology for monitoring fatigue cracks in steel bridges *Smart Mater. Struct.* **26** 085024
[49] Lu H, Dong P and Boppudi S 2015 Strength analysis of fillet welds under longitudinal and transverse shear conditions *Mar. Struct.* **43** 87–106
[50] PUGNO N, CIAVARELLA M, CORNETTI P and CARPINTERI A 2006 A generalized paris' law for fatigue crack growth *J. Mech. Phys. Solids* **54** 1333–49
[51] Allen R J, Booth G S and Jutla T 1988 A review of fatigue crack growth characterisation by linear elastic fracture mechanics lefm. Part (II) advisory documents and applications within national standards *Fatigue Fract. Eng. Mater. Struct.* **11** 71–108
[52] Broke D 2012 *The Practical use of Fracture Mechanics* (Galana, OH: FractuREsearch Inc.)
[53] Ritchie R 1999 Mechanisms of fatigue-crack propagation in ductile and brittle solids *Int. J. Fract.* **100** 55–83
[54] Kong X, Li J, Collins W, Bennett C, Laflamme S and Jo H 2017 A robust signal processing method for quantitative high-cycle fatigue crack monitoring using soft elastomeric capacitor sensors *Proc. SPIE* **10168** 101680B